# Modeling and Stability Analysis of Active Differential-Mode EMI Filters for AC/DC Power Converters

Rajib Goswami ⬡, *Student Member, IEEE* and Shuo Wang ⬡, *Senior Member, IEEE*

*Abstract*—In this paper, the active differential-mode (DM) electromagnetic interference (EMI) filter topology for ac/dc converters is first briefly investigated. The active DM EMI filter model was developed based on the models of filter components including a current transformer, a high-pass filter, an operational amplifier, and a class AB amplifier. The system model including the active filter, ac/dc converter, and line impedance stabilization networks (LISNs) are explored. With the developed system model, the loop gain and insertion gain of the active filter are derived. Based on the loop gain, the stability of the active filter is investigated and the compensation is applied to achieve stability and good EMI reduction. Both simulations and experiments are conducted to validate the developed technique.

*Index Terms*—AC/DC converter, differential-mode (DM) active filter, electromagnetic interference (EMI), stability.

## I. Introduction

**E**LECTROMAGNETIC Interference (EMI) is a big problem for power electronic circuits in modern days [1]. Switching-mode power conversion systems [2]–[5] are widely and increasingly used in various applications and are among major sources of EMI [4], [5]. The switching-mode power conversion systems employ pulse width modulation techniques with high switching frequencies and generate significant conducted EMI noise [4], [5]. The noise flowing between the power conversion systems and ground is usually called the common-mode (CM) noise and the noise flowing between two power carrying paths is called differential-mode (DM) noise [4], [5]. Different EMI regulations were developed to limit the emission from the power electronic circuits [1], [4]. These standards define the frequency range and the maximum magnitude of the EMI noise that is permissible. To combat the EMI issue and comply with the EMI standards, EMI filters are used. The commonly used filters are passive filters that constitute big inductors and capacitors [5].

Since the DM/CM inductors of the passive filter must carry the full-load current and the DM/CM capacitors may need to withstand high voltages, the passive filters can be very big and heavy [6]. In some applications, the passive EMI filters can take up to half of the size of the systems [5]. In order to reduce the size and weight of the EMI filters, hybrid EMI filters (HEF) that include an active filter and a small passive filter has been discussed in literatures [5]–[23].

In the HEF, the active EMI filter is designed for low-frequency (LF) noise reduction and the passive filter is designed for high-frequency (HF) noise reduction. Because of this, the passive filter's corner frequency can be increased and the size and weight can be greatly reduced [5]–[8]. At the same time, the HEF could achieve a good HF performance because the passive filter, which operates in the HF range, has small parasitic parameters [16].

However, most of the active and hybrid filter techniques, as found in the available literature, are either for dc/dc converters or for the EMI suppression on the dc side of dc/ac inverters [11], [12], [16], [20]. Moreover, almost all the HEF designs dealt with CM noise only [5], [6], [8]–[10], [16] and few papers dealt with DM noise [7], [17]–[21]. In [24], a general guideline is presented for passive DM EMI filter design. In [25] and [26], input passive DM EMI filter design method is presented after analyzing the worst EMI spectrum for a boost power factor correction (PFC) ac/dc converter. These papers give insights on passive DM EMI filter design for ac/dc converters. But, there are very few papers to address DM active EMI filters in the applications of ac/dc converters [18], [21], [22]. The active DM filter design on ac side is more challenging than the active DM filter design on dc side mostly because of stability issues [21], [22]. In [21] and [35], a topology has been developed to apply active filtering to the utility interface of a switching power supply. With their proposed topology, the difficulties involved in appropriately compensating a filter for a switching frequency of 75 kHz with substantial midband gain, as well as sufficiently low gain at the frequencies of the power line current, were shown impossible to overcome. However, it was shown in analysis and simulation that, with their topology, those difficulties can be solved at higher switching frequency of 450 kHz, when the band is wide enough to accommodate the LF roll off of the loop gain. In those works, for a selected topology, general analysis has been applied to

R. Goswami is with the University of Texas at San Antonio, San Antonio, TX 78249 USA (e-mail: rajibshohag@gmail.com).

S. Wang is with the University of Florida, Gainesville, FL 32611 USA (e-mail: shuowang@ieee.org).

check the viability of an active filter for low and high switching frequencies. However, detailed modeling of an active DM EMI filter was not done. Until now, a good modeling technique of an active DM EMI filter for ac/dc converters with quantitative analysis of stability and compensation design and successful hardware implementation results with a practical ac/dc converter has not been found in the available literatures. Hence, a good active filter modeling technique is needed to help understand the active filter system and to overcome all those issues.

In this paper, a hybrid DM EMI filter topology is presented for ac/dc converters. The passive filter topology that can improve the active filter's HF performance is first discussed. Second, the models of a current transformer (CT), an operational amplifier (OPAM), and a class AB amplifier are developed. The whole active filter's model is developed based on these models. Next, a system model, including the DM EMI noise model of an ac/dc converter, the model of an active DM EMI filter, and the model of line impedance stabilization networks (LISNs), has been developed. Based on the developed system model, the loop gain and insertion gains are derived for the active filter. The stability of the active filter is analyzed and the active filter is compensated to achieve both stability and good EMI reduction. The proposed technique has been theoretically analyzed and experimentally validated. Hence, in this paper, an active EMI filter model and compensation technique for DM noise of ac/dc converters will be developed. Almost all the available papers deal with CM noise, or DM noise in dc/dc converters, hence, the application of the model proposed in this paper is different. The specific contributions will be discussed in different sections in detail.

## II. ACTIVE DM EMI FILTER TOPOLOGY FOR AC/DC CONVERTERS

The active filter can be implemented either in feedback or feedforward configuration. In feedforward configuration, the unity gain of the active filter depends on the accuracy of filter component values [5], so it may not be convenient to achieve a good attenuation for mass production. Hence, in this paper, only feedback configuration will be analyzed. The analysis of feedforward is similar to the process developed in this paper.

There can be four different topologies of feedback active filters depending on what is sensed and what is injected [5]. A feedback active filter can sense either voltage or current and it can inject either voltage or current. A voltage injection active filter needs one voltage transformer for voltage injection. The voltage transformer is generally big due to the fact that full line currents must flow through one of its windings and its magnetizing inductance must be high enough to reduce magnetizing currents because the magnetizing currents lead to extra power loss in active filters. Because of these, voltage injection is not preferred. For the noise sensing, current sensing is preferred over voltage sensing in this paper, as it is convenient to separate DM noise currents from CM currents using a current transformer (CT); on the other hand, the voltage sensing needs to separate DM noise voltages from CM voltages.
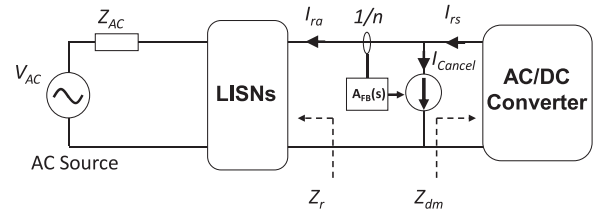


Fig. 1.    Feedback hybrid DM filter topology for an ac/dc converter with LISNs connected between the ac source and the ac/dc converter.
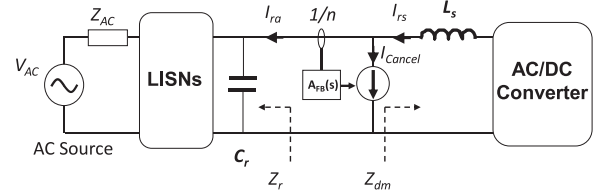


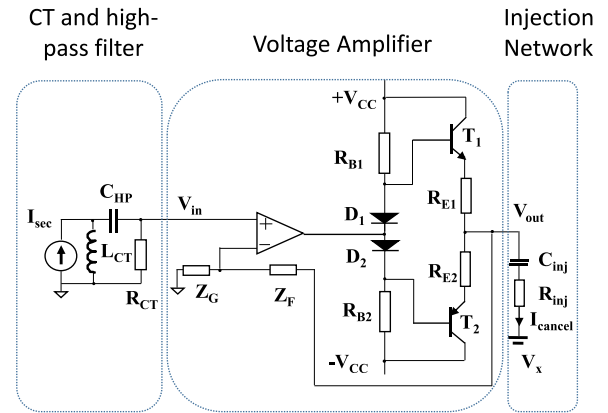Fig. 2.    Preferred hybrid current injection EMI filter topology.



Fig. 3.    Active filter circuit under investigation.

Based on the above-mentioned analysis, the feedback hybrid DM filter topology to be investigated is shown in Fig. 1. For current injection, a big noise source impedance $Z_{dm}$ and a small load impedance $Z_r$ are preferred for the active filter [5]. If this impedance condition does not meet, a series inductor should be added between the active filter and the ac/dc converter, and a shunt capacitor should be added between the active filter and the ac sources or LISNs (shown in Fig. 2).

The circuit of the active filter in Figs. 1 and 2 is shown in Fig. 3. In Fig. 3, the current sensing and current injection active filter consists of a current sensing and high-pass filter (HPF) function block, a voltage amplifier function block, and an injection network block.

A CT is used to sense noise currents and a second-order HPF, which is composed of $L_{CT}$, $C_{HP}$, and $R_{CT}$, is used to reject the sensed LF currents, including line-frequency currents, below the concerned frequency ranges in EMI standards. The HPF is necessary as the active filter should not inject the cancelation currents to cancel the LF currents, otherwise high power loss will be generated in the active filter. This is especially true

for the line-frequency currents because they usually have large magnitude as they carry the power currents.

The voltage amplifier includes an OPAM and a class AB current amplifier. $Z_F$ and $Z_G$ have a voltage feedback, which determines the gain and phase of the amplifier for stable operation. $R_{B1}, R_{B2}, D_1$, and $D_2$ are the dc bias circuit of the class AB amplifier. $R_{E1}$ and $R_{E2}$ are the emitter resistance for negative thermal feedback to solve class AB amplifier's thermal runaway issue.

The current injection network consists of an injection capacitor, $C_{inj}$ and an injection resistor $R_{inj}$. It has the following three functions:

1) $C_{inj}$ is needed for the isolation of the active filter from high-voltage ac input;
2) $C_{inj}$ and $R_{inj}$ also generate a first-order HPF to further reduce the undesired injection currents below the concerned frequency range in EMI standards; and
3) at frequencies higher than the corner frequency of the HPF, $R_{inj}$ helps to keep a constant impedance for the injection network.

The active filter model will be developed in Section III, and its loop gain and insertion gain in feedback configuration will be derived in Section IV. In Section V, the active filter's stability will be discussed based on the derived loop gain and compensation will be applied to achieve stability and good EMI reduction. Experiments will be conducted to validate the developed techniques in this paper. Finally, conclusion is presented in Section VI.

## III. DEVELOP THE ACTIVE FILTER MODEL

In this section, the models of critical components in the active filter will be developed and verified. These critical components include the CT and the HPF, the OPAM, and the class AB amplifier.

### A. CT and HPF Model

Moreover, the active filter for ac/dc converters must have HPF to reject the LF line currents, but this introduces stability issues. In [21], an inductor has been used in the noise sensing part as a simple HPF. But, it did not have a control over the corner frequency of the HPF and tried to solve the stability issue at the LF crossover of loop gain by using a compensation network with the amplifier. Hence, when the switching frequency was low, Farkas and Schlecht [21] could not solve the stability issue while trying to maintain substantial midband gain, as well as sufficiently low gain at the frequencies of the power line current. In this paper, the corner frequency of the HPF can be designed based on the parameters of CT and the HPF capacitor. Hence, the corner frequency can be designed to achieve enough phase margin of the loop gain at LF crossover.

The CT and HPF are included in the model of the active filter. Based on the active filter model, the CT and HPF block can be designed to ensure LF stability. Only stability issues at HF crossover needs to be compensated by the OPAM.

The CT under investigation in Fig. 4(a) has a turn ratio of $1:n$, where $n = 10$. The CT can be modeled as a current source
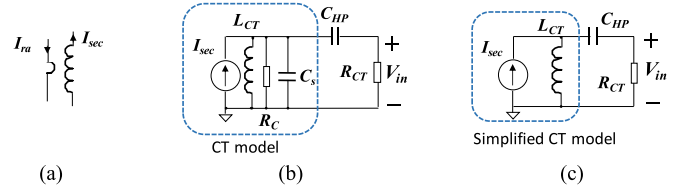


Fig. 4. CT model: (a) CT under investigation, (b) CT model with $C_{HP}$ and $R_{CT}$ referred to secondary, and (c) simplified CT model with $C_{HP}$ and $R_{CT}$.
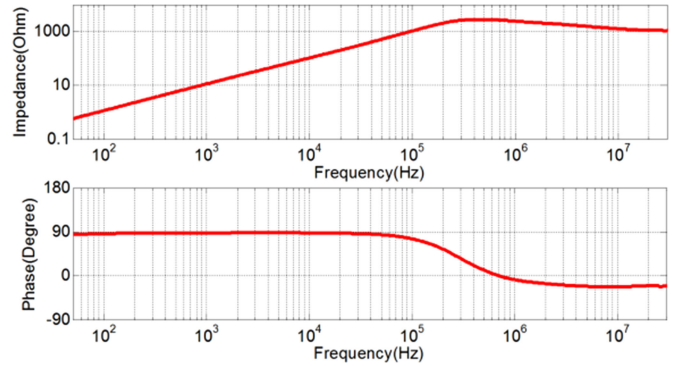


Fig. 5. Magnitude and phase of the measured impedance.

$I_{sec}$ in parallel with an *LRC* network, as shown in Fig. 4(b) [16]. $I_{sec}$ is the reflected noise current from the primary winding and it is equal to $I_{ra}/n$, where $I_{ra}$ is the noise current in the primary winding. $L_{CT}$ is the magnetizing inductance of the CT. $R_C$ represents the core loss and $C_s$ represents the winding capacitance. They can be extracted through the measured secondary winding impedance of the CT. The magnitude and phase of the measured impedance, $Z_{CT}$ from 50 Hz to 30 MHz, are shown in Fig. 5. From the impedance curve of $Z_{CT}$ in Fig. 5, at the low frequencies, where the phase is 90°, $L_{CT}$ can be approximately found from $Z_{CT} = 2\pi f \times L_{CT}$. At the corner frequency, when the phase of the impedance is zero, $f_c = \frac{1}{2\pi\sqrt{L_{CT}C_s}}$. Hence, $C_s$ can be calculated from this equation. At this resonance frequency, $Z_{CT} = R_c$. Hence, based on the measured impedance curves, for the first-order approximation, $L_{CT} = 1.96 \text{ mH}, R_C = 2.8 \text{ k}\Omega$, and $C_s = 26.375 \text{ pF}$. The output of the CT is connected to high-pass capacitor $C_{HP} = 1.1 \mu\text{F}$ and load resistor $R_{CT} = 30 \Omega$.

At first, leakage inductance $L_{leak}$ and parasitic resistance of the CT secondary inductance $R_C$ and parasitic capacitance $C_s$ were included in the model. Later it was found that in the concerned frequency range, CT can be modeled with a simpler model, as shown in Fig. 4(c), as the impedances of $R_C$ and $C_s$ are much larger than the impedances of $L_{CT}$ below HPF's corner frequency $f_{HP} = 3.4 \text{ kHz}$, which is determined by $L_{CT}$ and $C_{HP}$, and much larger than the impedance of $C_{HP}$ and $R_{CT}$ from 100 kHz to 30 MHz. For the CT, the secondary leakage inductance has been measured as $L_{leak} \approx 0.4 \mu\text{H}$, and in the concerned frequency range, its impedance is small compared to $R_{CT}$. Hence, it was ignored in the model.

The measured impedance in Fig. 5 shows that as the phase is close to zero at the high frequencies, because of the power
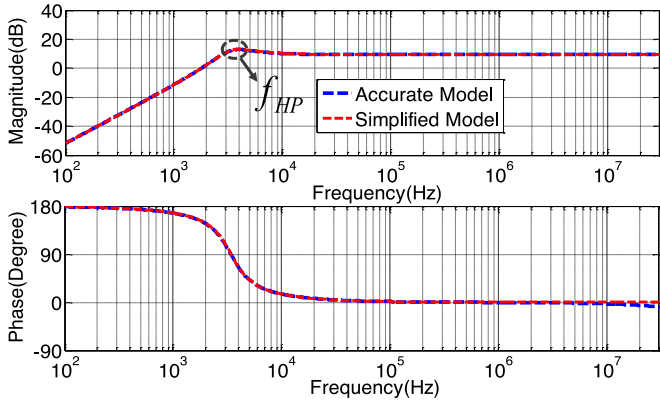
Fig. 6. Comparison of the transfer gains derived from the models in Fig. 4(b) and (c).
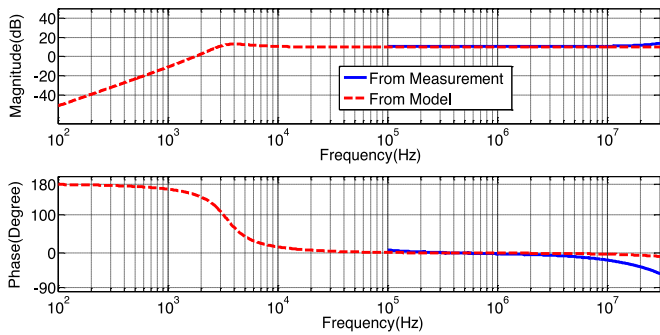


Fig. 7. Comparison of CT's transfer gains derived from measured $S$-parameters and the simplified CT model.

loss in the core, the impedance is still high. Hence, even though the permeability of the CT core is reduced, most of the current still flows to CT's load impedance $Z_{\mathrm{CHP}} + R_{\mathrm{CT}}$, which is much smaller than the CTs impedance and the reduced permeability does not affect the sensed current (which is validated in the measurement in Fig. 7).

The transfer gain from the current $I_{\mathrm{ra}}$ on CT's primary winding to the output voltage $V_{\mathrm{in}}$ on CT's load $R_{\mathrm{CT}}$ is given by the following equation:

$$\frac{V_{\mathrm{in}}(s)}{I_{\mathrm{ra}}(s)} = \frac{\left(\frac{s}{\omega_{\mathrm{HP}}}\right)^2 \frac{R_{\mathrm{CT}}}{n}}{1 + \frac{s}{\omega_{\mathrm{HP}} Q} + \left(\frac{s}{\omega_{\mathrm{HP}}}\right)^2} \qquad (1)$$

where $\omega_{\mathrm{HP}} = \frac{1}{\sqrt{L_{\mathrm{CT}} C_{\mathrm{HP}}}}$ and $Q = \frac{1}{R_{\mathrm{CT}}}\sqrt{\frac{L_{\mathrm{CT}}}{C_{\mathrm{HP}}}}$. The corner frequency $f_{\mathrm{HP}}$ of HPF is 3.4 kHz. The transfer gains derived from the models in Fig. 4(b) and (c) are compared in Fig. 6. They match very well, so the simplified model in Fig. 4(c) is accurate enough.

To further validate the simplified model in Fig. 4(c), a $2 \times 2$ $S$-parameter matrix $(S_{11}, S_{12}, S_{21}, S_{22})$ was measured between CT's primary winding (port 1) and output (port 2) with the load resistor $R_{\mathrm{CT}}$ connected using network analyzer Copper Mountain Planar 808/1. Based on the measured $S$-parameters, the CT's input current to the output voltage gain can be calculated
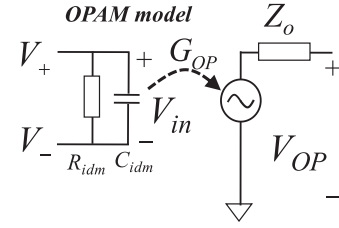
based on the technique in [16], [27], and [28]. The gain calculated based on the measured $S$-parameters was compared with that derived from the CT model in Fig. 7. They match very well below 10 MHz. There is a small difference between 10 and 30 MHz. Because the lowest frequency, which the network analyzer can measure, is 100 kHz, the measured curve starts from 100 kHz.



Fig. 8. Comparison of the transfer gains derived from the models in Fig. 4(b) and (c).

### B. OPAM Model

In [16], a simplified OPAM model was derived. In this paper, due to the necessity of injecting higher current, a class AB current amplifier had to be used. Modeling the active EMI filter with OPAM and class AB amplifier including all the parasitic parameters of both is a contribution of this paper. This helps to analyze the effect of their parasitic parameters related to the HF stability issues. Some other papers have used the class AB amplifier to increase the current injection capacity [5], but did not model the class AB amplifier along with the OPAM to find their effect in the HF stability. In this section, an OPAM is modeled, and in the next section, class AB amplifier combined with OPAM shall be modeled.

*1) Open-Loop Transfer Function of OPAM:* In [16], a four-stage OPAM model was introduced. The four stages include input stage, slew-rate limiting and dominant pole stage, unity gain and higher pole stage, and output stage. It has been shown in [16] that the equivalent circuit of the OPAM can be simplified to the model in Fig. 8.

In Fig. 8, $G_{\mathrm{OP}}$ is the open-loop gain of the OPAM. $R_{i\mathrm{dm}}, C_{i\mathrm{dm}}$, and $Z_o$ are the input resistance, the input capacitance, and the output impedance of the OPAM, respectively. $V+$ and $V-$ are the input voltages in the two input pins and $V_{\mathrm{OP}}$ is the open-loop output voltage of the amplifier. The open-loop gain $G_{\mathrm{OP}}$ can be expressed as

$$G_{\mathrm{OP}} = \frac{V_{\mathrm{OP}}}{V_{\mathrm{in}}} = \frac{G_o}{\left(1 + \frac{s}{\omega_1}\right)\left(1 + \frac{s}{\omega_2}\right)}. \qquad (2)$$

$G_{\mathrm{OP}}$ contains three parameters, $G_o, \omega_1$, and $\omega_2$. These parameters can be either found in the datasheet of an OPAM or from measurements. The OPAM used in this paper is AD829, a conventional voltage feedback amplifier. Based on its datasheet [29], the phase and the gain of its open-loop transfer function are shown in Fig. 9(a) and the dc gain $G_o$ as a function of load resistance is given in Fig. 9(b). The OPAM uses $\pm 15$ V power
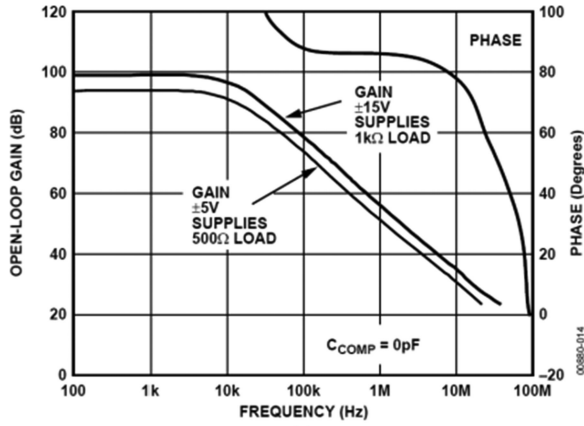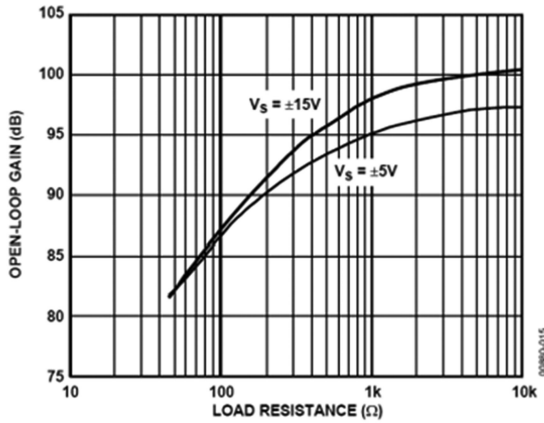
Fig. 9.    Characteristics of OPAM. (a) Magnitude and phase of the open-loop gain. (b) Open-loop gain versus load resistance [29].
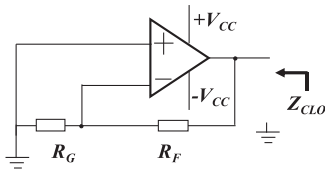


Fig. 10.    Closed-loop output impedance measurement.

supply, so the 15-V gain curves will be used to determine poles, zeros, and dc gains.

Based on the gain and phase curves, there is a pole $\omega_1$ around 10 kHz and several poles and zeros at high frequencies. Because conductive EMI is concerned with the active filter, only the lowest pole $\omega_2 \approx 35$ MHz above 30 MHz is considered and other poles and zeros above 30 MHz are ignored. $G_o$ is determined based on the load. The closed-loop output impedance $Z_{\mathrm{CLO}}$, shown in Fig. 10, can be measured with an impedance or $S$-parameter analyzer. The closed-loop output impedance curve is given in the datasheet [29] for a gain of +20. Hence, for this measurement, $R_G = 500\,\Omega$ and $R_F = 10\,\mathrm{k}\Omega$ have been used to match the measurement in the datasheet.

The measured closed-loop impedance and that given in the datasheet are shown in Fig. 11. Only the measured phase is
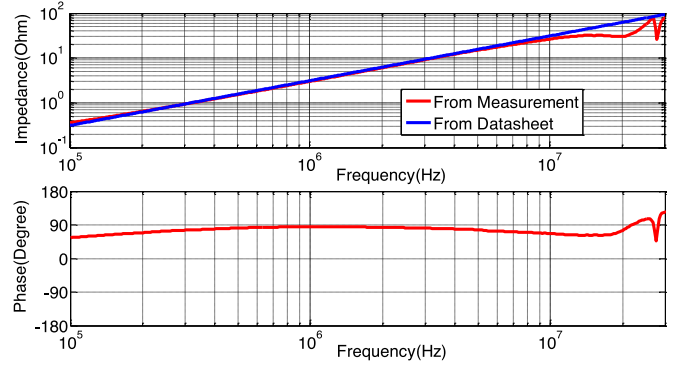


Fig. 11.    Closed-loop output impedance magnitude and phase from the measurement and datasheet.
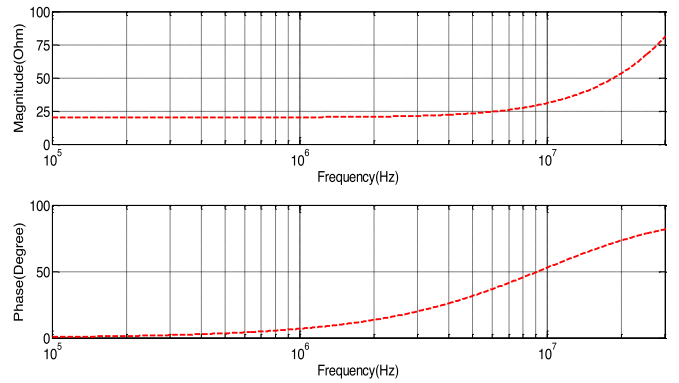


Fig. 12.    Calculated open-loop output impedance from the closed-loop impedance curve given in the datasheet.

shown in Fig. 11, as the datasheet includes the magnitude of the impedance only.

From the closed-loop output impedance in Fig. 11, the open-loop output impedance $Z_o$ can be derived in (3) based on Fig. 10 and (2). The derived $Z_o$ is shown in Fig. 12.

$$Z_o = Z_{\mathrm{CLO}} \left( 1 + \left( \frac{R_G}{R_G + R_F} \right) G_{\mathrm{OP}} \right). \tag{3}$$

It was found that $Z_o$ can be approximately represented with a 20-$\Omega$ resistance below 10 MHz. Above 10 MHz, it is not so accurate. A resistance in series with an inductance can be a more accurate model for $Z_o$, but it will make the system model much more complicated and difficult to analyze, so a simple 20-$\Omega$ resistance is used in this paper.

Based on these parameters, the model of the OPAM was developed. To validate the developed OPAM model, a noninverting configuration shown in Fig. 13(a) was tested in the experiments. $R_G$, $R_F$, and $R_L$ are 1 k $\Omega$, 10 k$\Omega$, and 1 k$\Omega$, respectively. Based on Figs. 8 and 13(a) and (4), the following equation can be derived for the voltage gain [30]

$$A_{\mathrm{VOP}} = \frac{V_o}{V_{\mathrm{in}}} = \frac{\frac{G_{\mathrm{OP}}}{Z_o}}{\frac{1}{Z_o} + \frac{1}{R_L} + \frac{1}{R_G + R_F} + \frac{R_G}{R_G + R_F} \times \frac{G_{\mathrm{OP}}}{Z_o}}. \tag{4}$$
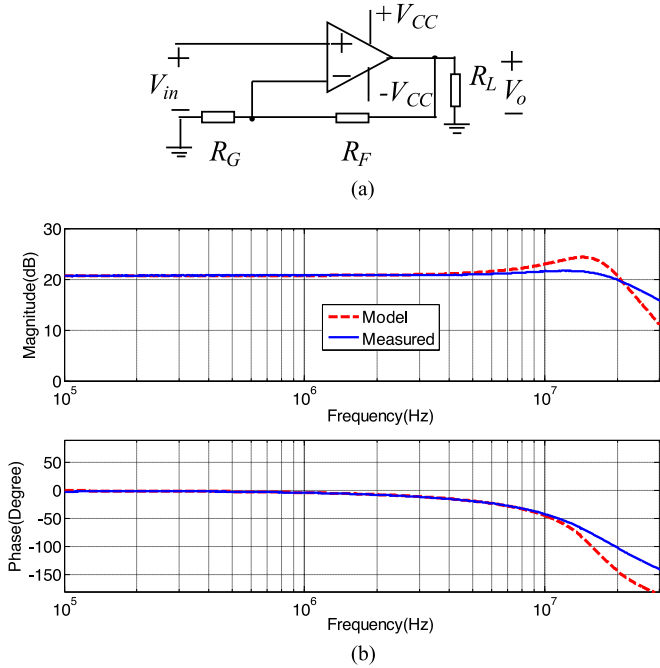
(a)



(b)

Fig. 13. Validation of the developed OPAM model. (a) Noninverting Op-amp circuit used to validate the developed OPAM model. (b) Comparison of the measured gain and the predicted gain based on the model.

The voltage gain is predicted based on the developed model (4). At the same time, the $S$-parameter matrix of this network was measured using a network analyzer with $R_L$ included and the voltage gain of the OPAM circuit was derived based on the measured $S$-parameters with a technique similar to that in [16], [27], and [28].

The predicted voltage gain based on (4) and the measured voltage gain are compared in Fig. 13(b). It is shown that two results match well. This validates the developed OPAM model.

## C. Model of Class AB Amplifier With OPAM

A class AB amplifier has been used in the output stage of the active filter circuit to amplify the injection current, as shown in Fig. 3. The class AB amplifier has a matched npn–pnp complementary transistor pair ZDT6753. The small signal model of the class AB amplifier together with the OPAM is shown in Fig. 14. There is only one transistor model used in Fig. 14 because the transistor pair has an almost symmetric model structure and there is only one transistor conducting current at the same time.

In Fig. 14, $V_B, V_E$, and $V_C$ are base, emitter, and collector voltages, respectively, $R_B$ is the biasing resistance at the base, and from Fig. 3, $R_B = R_{B1} \| R_{B2}, R_E$ is the emitter resistance, $R_{BE}$ is base to emitter resistance, $C_{BE}$ is base to emitter capacitance, $C_{BC}$ is base to collector capacitance, $r_o$ is the output resistance of the transistor, $g_m$ is the transconductance, and the transistor current gain $\beta = g_m Z_{BE}$. $Z_{BE}$ is $R_{BE}$ and $C_{BE}$ in parallel. $Z'_o$ is the open-loop output impedance of the whole configuration and $V'_{OP}$ is the open-loop output voltage. The relation
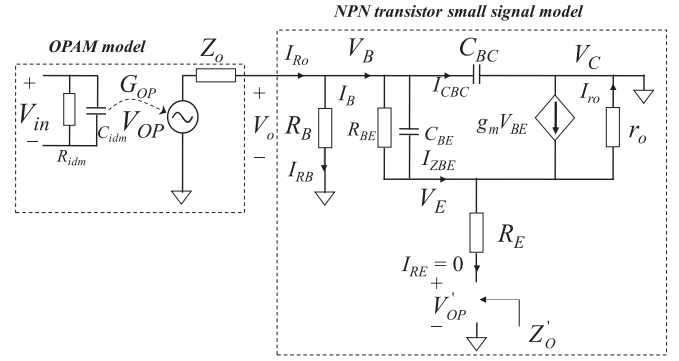


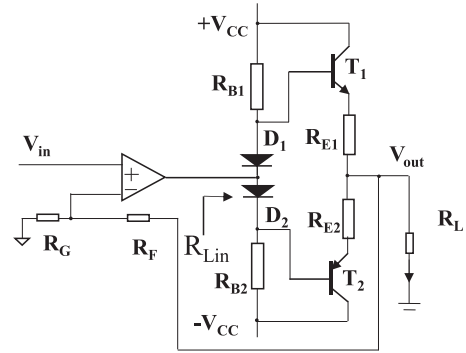Fig. 14. Small signal model of the class AB amplifier together with the OPAM.



Fig. 15. Validation of the model including both OPAM and class AB amplifier using a noninverting configuration.

between $V_{OP}$ and $V'_{OP}$ can be derived as follows:

$$\frac{V'_{OP}}{V_{OP}} = \frac{K_P}{1 + \frac{s}{\omega'_{PBC}}}. \tag{5}$$

Here, $K_P = \frac{R_P}{Z_o + R_P}$, $\omega'_{PBC} = \omega_{PBC} \times (1 + \frac{R_P}{Z_o})$, $\omega_{PBC} = \frac{1}{C_{BC} \times R_P}$, and $\frac{1}{R_P} = \frac{1}{r_o(\beta+1)} + \frac{1}{R_B}$.

The expression for $Z'_o$ can be derived as follows:

$$Z'_o = R_E + \frac{(Z_{Z_o C_{BC}} + Z_{BE}) \times r_o}{(\beta + 1) \times r_o + Z_{Z_o C_{BC}} + Z_{BE}}. \tag{6}$$

Here, $Z_{Z_o C_{BC}} = Z_o \| R_B \| \frac{1}{sC_{BC}}$ and $Z_{BE} = R_{BE} \| \frac{1}{sC_{BE}}$.

Equations (5) and (6) are the math model for Fig. 14. To validate the model, a noninverting configuration including both OPAM and class AB amplifier shown in Fig. 15 was tested in the experiments. $R_G, R_F$, and $R_L$ are 1 k$\Omega$, 10 k$\Omega$, and 20 $\Omega$, respectively. $R_{B1}$ and $R_{B2}$ are 4.7 k$\Omega$ and the biasing $D_1$ and $D_2$ diodes used are 1N4148 high-speed signal diodes. Both $R_{E1}$ and $R_{E2}$ are 5-$\Omega$ resistors and used for thermal stability. The model parameters from the datasheet and measurement extraction based under dc bias $V_{CC} = 15$ V and $I_B = 1.1$ mA are $C_{BC} = 30$ pF, $C_{BE} = 300$ pF, $R_{BE} = 469 \,\Omega$, $r_o = 20.3$ k$\Omega$, $g_m = 0.32$, and $\beta = 150$. In Fig. 15, $R_{Lin}$ is the load resistance seen by the OPAM with the class AB amplifier stage added and $R_{Lin} \approx R_{BE} + (\beta + 1)(R_E + R_L)$, where $R_F + R_G >> R_L$. Based on $R_{Lin}$, the dc gain $G_o$ in (3) can be determined from Fig. 9(b).
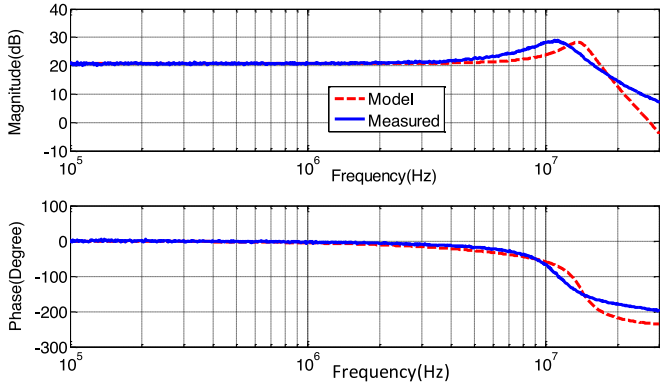
Fig. 16. Comparison of the measured and the predicted gains for the OPAM-Class AB amplifier configuration of Fig. 15.



Fig. 17. System under investigation.



Fig. 18. DM EMI noise model of an ac/dc converter with Norton equivalence.

Based on the model (5), (6) and the circuit in Fig. 15, the following equation can be derived for the voltage gain of the noninverting configuration in Fig. 15:

$$A_V = \frac{V_{\text{out}}}{V_{\text{in}}} = \frac{\frac{G'_{\text{OP}}}{Z'_o}}{\frac{1}{Z'_o} + \frac{1}{R_L} + \frac{1}{R_G + R_F} + \frac{R_G}{R_G + R_F} \times \frac{G'_{\text{OP}}}{Z'_o}} \quad (7)$$

where $G'_{\text{OP}} = G_{\text{OP}} \times \frac{K_P}{1 + \frac{s}{\omega'_{\text{PBC}}}}$ is the open-loop voltage gain without load $R_L$. The predicted gain using (7) and the measured gain using $S$-parameters are compared in Fig. 16. It is shown that two results match well. This validates the model (7).

Based on (7), when $R_L = \infty$, the transfer function $V_{\text{out}}/I_{\text{ra}}$ of the whole active filter, which includes a CT, an HPF, an OPAM, and a class AB amplifier, is derived in (8), where $I_{\text{ra}}$ is the sensed noise current. Because $R_L = \infty$, $V_{\text{out}}$ is the Thevenin equivalent output voltage of the active filter

$$A_{\text{VFB}}(s) = \frac{V_{\text{out}}(s)}{I_{\text{ra}}(s)} = \frac{\left(\frac{s}{\omega_{\text{HP}}}\right)^2 \frac{R_{\text{CT}}}{n}}{1 + \frac{s}{\omega_{\text{HP}} Q} + \left(\frac{s}{\omega_{\text{HP}}}\right)^2}$$

$$\times \frac{\frac{G'_{\text{OP}}}{Z'_o}}{\frac{1}{Z'_o} + \frac{1}{R_G + R_F} + \frac{R_G}{R_G + R_F} \times \frac{G'_{\text{OP}}}{Z'_o}}. \quad (8)$$

If (3) is applied to the whole active filter, the Thevenin equivalent output impedance $Z'_{\text{CLO}}$ of the active filter can be derived as follows:

$$Z'_{\text{CLO}} = \frac{Z'_o}{\left(1 + \left(\frac{R_G}{R_G + R_F}\right) G'_{\text{OP}}\right)}. \quad (9)$$

## IV. DEVELOP A SYSTEM MODEL FOR ACTIVE DM EMI FILTERS WITH AC/DC CONVERTERS

Because the active DM EMI filter is going to be used between the ac power line and an ac/dc power converter, to analyze the active filter performance and develop a design technique to achieve stability, a model, including an active filter, a noise source, and a load, must be developed first.
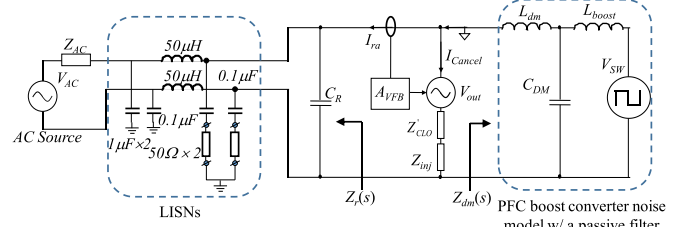
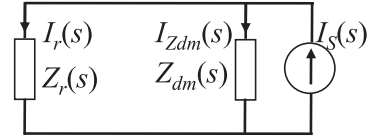Because LISNs are used between the ac power line and active DM EMI filter for EMI measurement, the impedance of LISNs will be treated as the load of the active filter in a standard EMI measurement setup. The single-phase ac/dc converter can be viewed as the DM noise voltage source with its equivalent source impedance for the active filter. When there is a passive EMI filter before the converter, the passive EMI filter should be included in the model. The system under investigation is shown in Fig. 17. It includes a front-end boost PFC converter, a passive filter, the active filter, and LISNs. The boost PFC converter in Fig. 17 is modeled with a noise source impedance, which is the impedance of the boost inductor $L_{\text{boost}}$, and a noise voltage source $V_{\text{SW}}$, which is the voltage of the main switch [31], [32]. There is a passive EMI filter before the boost PFC converter. $C_{\text{DM}}$ is the passive filter DM capacitance. $L_{\text{dm}}$ is the passive filter DM inductance that includes the total DM inductance of DM inductor and the leakage of CM inductor. $C_R$ is a passive filter capacitor. The active filter is added in between the DM inductor $L_{\text{dm}}$ and $C_R$ to meet the impedance requirement [5] for high performance. After $C_R$, there are two LISNs in series for DM noise. They can be modeled as a single equivalent impedance.

The noise model for the boost PFC converter together with $C_{\text{DM}} - L_{\text{dm}}$ can be modeled using a Norton equivalent current source $I_s(s)$ and a Norton equivalent parallel impedance $Z_{\text{dm}}(s)$, as shown in Fig. 18. $Z_{\text{dm}}(s)$ is the equivalent output impedance defined in Fig. 17. $Z_r(s)$ is the equivalent load impedance of the active filter, as defined in Fig. 17. $I_{\text{ra}}(s)$ is the current flowing through $Z_r(s)$. The Norton equivalence is used because it is convenient to derive current transfer functions.

Based on the Norton equivalent model in Fig. 18, the current gain $G_{\text{OL}}(s) = \frac{I_r(s)}{I_s(s)}$ before the insertion of an active filter can be derived as follows:

$$G_{\text{OL}}(s) = \frac{Z_{\text{dm}}}{Z_{\text{dm}} + Z_r}. \quad (10)$$

With the feedback active filter inserted between $C_R$ and $L_{\text{dm}}$ in Fig. 17, the system model including the active filter can be derived in Fig. 19, with a current sensing-current injection
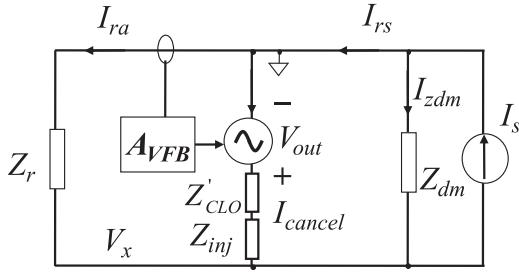
Fig. 19. Current sensing-current injection feedback active filter along with the DM EMI noise model of an ac/dc converter.
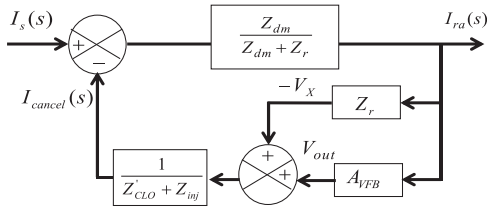


Fig. 20. Closed-loop signal flow diagram of the current sensing-current injection feedback active filter.

feedback configuration. In Fig. 19, as derived in Section III, $V_{\text{out}}$ and $Z'_{\text{CLO}}$ are the Thevenin equivalent voltage source and output impedance, respectively. $A_{\text{VFB}}(s)$ is also derived in Section III. $Z_{\text{inj}}$ is the injection impedance, which is $C_{\text{inj}}$ and $R_{\text{inj}}$ in series, as shown in Fig. 3. $I_{\text{ra}}$ is the current flowing through $Z_r$ after the insertion of the active filter and $I_{\text{rs}}$ is the output current of the Norton equivalent noise source. $I_{\text{cancel}}$ is the cancelation current injected by the active filter. The ground of the active filter is connected to one (top) of the two ac lines and $Z_{\text{inj}}$ is connected to the other ac line, so the $I_{\text{cancel}}$ can flow between two ac lines to cancel DM noise current, as shown in Fig. 19. The ground of the active filter is also the reference ground of the whole system for the later analysis. And the voltage of the other (bottom) line is $V_x$.

Based on Fig. 19, the following equations can be derived as follows:

$$I_{\text{rs}}(s) = I_{\text{cancel}}(s) + I_{\text{ra}}(s) \tag{11}$$

$$(I_s(s) - I_{\text{cancel}}(s)) \times G_{\text{OL}}(s) = I_{\text{ra}}(s) \tag{12}$$

$$V_x = -I_{\text{ra}}(s) \times Z_r \tag{13}$$

$$I_{\text{cancel}}(s) = \frac{I_{\text{ra}}(s) \times A_{\text{VFB}}(s) + I_{\text{ra}}(s) \times Z_r}{Z'_{\text{CLO}} + Z_{\text{inj}}}. \tag{14}$$

The closed-loop signal flow diagram for the model of Fig. 19 can be derived based on (11)–(14) in Fig. 20.

To derive the loop gain of the active filter, one of the feedback paths $Z_r/(Z'_{\text{CLO}} + Z_{\text{inj}})$ should be combined with the forward path because it is due to the circuit connection instead of the action of the active filter. In [16], the loop gain was derived based on transfer gain equation, but from transfer gain equation, there are different possible loop gain equations, however, only one of which is correct. In this paper, the feedback path and forward path are identified. Because the feedback path is due to the active
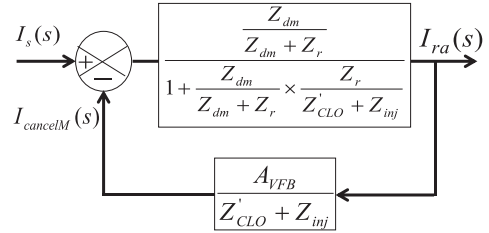


Fig. 21. Simplified signal flow diagram.

filter only, when the active filter is connected but not powered, then gain should not be included in the loop gain and should be with the forward gain. So, the correct loop gain can be identified. Fig. 20 can be further simplified to Fig. 21 based on the signal flow theory. Here, $I_{\text{cancelM}}(s)$ is an intermediate signal used in the derivation. Moreover, $G'_{\text{OL}}(s) = \frac{\frac{Z_{\text{dm}}}{Z_{\text{dm}}+Z_r}}{1+\frac{Z_{\text{dm}}}{Z_{\text{dm}}+Z_r}\times\frac{Z_r}{Z'_{\text{CLO}}+Z_{\text{inj}}}}$ is the forward path gain.

The closed-loop transfer function $G_{\text{FB}}(s)$, which is the ratio of $\frac{I_{\text{ra}}(s)}{I_s(s)}$, can be derived as follows:

$$G_{\text{FB}}(s) = \frac{I_{\text{ra}}(s)}{I_s(s)} = \frac{G'_{\text{OL}}(s)}{1 + T_{\text{FB}}(s)} \tag{15}$$

where $T_{\text{FB}}(s)$ is the loop gain for the closed-loop feedback active filter, which can be used to determine the closed-loop stability. From Fig. 21, the loop gain is derived by multiplying the forward path gain and feedback path gain. Hence

$$T_{\text{FB}}(s) = \frac{\frac{Z_{\text{dm}}}{Z_{\text{dm}}+Z_r}}{1+\frac{Z_{\text{dm}}}{Z_{\text{dm}}+Z_r}\times\frac{Z_r}{Z'_{\text{CLO}}+Z_{\text{inj}}}} \times \frac{A_{\text{VFB}}}{Z'_{\text{CLO}}+Z_{\text{inj}}}. \tag{16}$$

The insertion gain $G_{\text{IFB}}$, which is defined as the current ratio of the current flowing through $Z_r$ with the active filter in Fig. 19 and that without the active filter in Fig. 18, can be derived as follows:

$$
\begin{aligned}
G_{\text{IFB}}(s) &= \frac{G_{\text{FB}}(s)}{G_{\text{OL}}(s)} = \frac{I_{\text{ra}}(s)}{I_r(s)} = \frac{1}{G_{\text{OL}}(s)} \times \frac{G'_{\text{OL}}(s)}{1+T_{\text{FB}}(s)} \\
&= \frac{1}{G_{\text{OL}}(s)} \times \frac{G_{\text{OL}}(s)}{1+G_{\text{OL}}(s)\times\frac{A_{\text{VFB}}+Z_r}{Z'_{\text{CLO}}+Z_{\text{inj}}}} \\
&= \frac{1}{1+G_{\text{OL}}(s)\times\frac{A_{\text{VFB}}+Z_r}{Z'_{\text{CLO}}+Z_{\text{inj}}}}. \tag{17}
\end{aligned}
$$

In (17), the loop gain $T_{\text{FB}}(s)$ should be as big as possible to reduce $G_{\text{IFB}}$. Moreover, to ensure stability, the loop gain must have sufficient gain and phase margins at both LF and HF crossovers. The closed-loop stability of the feedback active filter can be analyzed based on the component models derived in the previous section and the loop gain derived in this section.

## V. STABILITY ANALYSIS, COMPENSATION, AND EXPERIMENTAL RESULTS

In this section, the loop gain and insertion gain models developed in Section IV will be validated and analyzed. The stability of a system including a feedback active filter and an ac/dc
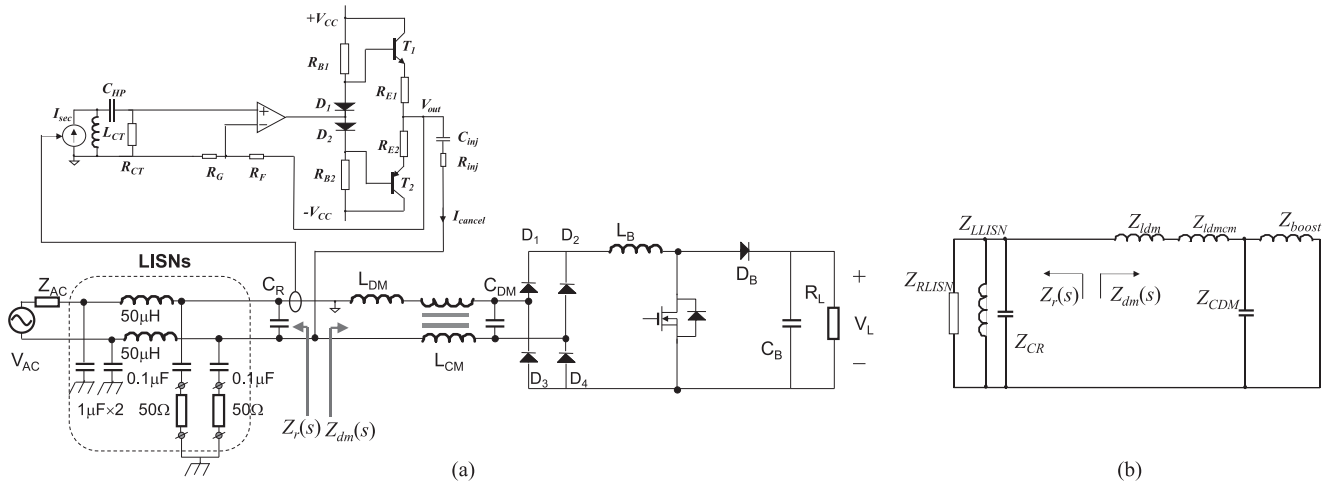
Fig. 22. Stability analysis. (a) System under investigation. (b) Source and load impedances of the active filter.

boost PFC converter will be investigated based on the developed model. The active filter will be compensated to achieve stability based on the developed model, noise source, and load impedances. The EMI measurement will be conducted to verify that the compensated active filter can achieve both DM EMI reduction and stable operation.

## A. Stability Analysis

In Fig. 22(a), the feedback active filter is inserted between the boost converter and the LISNs. There are a DM inductor $L_{\mathrm{DM}}$, a CM inductor $L_{\mathrm{CM}}$, and a DM capacitor $C_{\mathrm{DM}}$ between the boost PFC converter and the active filter. The DM capacitor $C_{\mathrm{R}}$ is between the active filter and the LISNs to meet the impedance requirement as described previously. The noise model of the boost PFC converter is modeled with its Norton equivalence, as shown in Fig. 18. $Z_r$ and $Z_{\mathrm{dm}}$ can be determined in Fig. 22(b), as shown in the figure. Based on Fig. 22(b), $Z_{\mathrm{dm}}(s) = Z_{\mathrm{ldm}}(s) + Z_{\mathrm{ldmcm}}(s) + Z_{\mathrm{boost}}(s) || Z_{\mathrm{CDM}}(s)$, where $Z_{\mathrm{ldm}}(s)$ is the impedance of the DM inductor and $Z_{\mathrm{ldmcm}}(s)$ is the DM impedance of the CM inductor; $Z_{\mathrm{boost}}(s)$ and $Z_{\mathrm{CDM}}(s)$ are impedances of the boost inductor and the DM filter capacitor, respectively. The measured DM inductor impedance $Z_{\mathrm{ldm}}$ is $L_{\mathrm{ldm}} = 71\,\mu\mathrm{H}$ with parasitic resistance $R_{\mathrm{ldm}} = 5.42\,\mathrm{k\Omega}$, and parasitic capacitance $C_{\mathrm{ldm}} = 6.1\,\mathrm{pF}$ in parallel. The measured DM impedance $Z_{\mathrm{ldmcm}}$ of the CM inductor is $L_{\mathrm{ldmcm}} = 23.6\,\mu\mathrm{H}$ with parasitic resistance $R_{\mathrm{ldmcm}} = 3\,\mathrm{k\Omega}$, and parasitic capacitance $C_{\mathrm{ldmcm}} = 0.28\,\mathrm{nF}$ in parallel. The impedance of the boost inductors is $L_{\mathrm{boost}} = 327\,\mu\mathrm{H}$, with parasitic resistance $R_{\mathrm{boost}} = 2.97\,\mathrm{k\Omega}$, and parasitic capacitance $C_{\mathrm{boost}} = 9.44\,\mathrm{nF}$ in parallel. The DM filter capacitor's impedance is determined by $C_{\mathrm{DM}} = 0.2\,\mu\mathrm{F}$ as it has very small parasitic inductance and resistance. The calculated and the measured noise source impedance $Z_{\mathrm{dm}}$ are compared in Fig. 23. They match very well in both magnitude and phase. It is shown that $Z_{\mathrm{dm}}$ is dominated by $L_{\mathrm{ldm}} + L_{\mathrm{ldmcm}} + L_{\mathrm{boost}}$ below 20 kHz, by $C_{\mathrm{DM}}$ between 20 and 40 kHz, by $L_{\mathrm{ldm}} + L_{\mathrm{ldmcm}}$ bewteen 40 kHz and 2 MHz, by $L_{\mathrm{ldm}}$
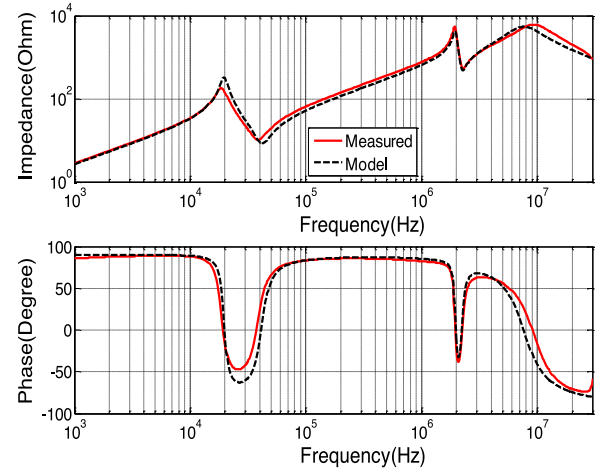


Fig. 23. Comparison of the measured and modeled $Z_{\mathrm{dm}}$(s).

between 2 and 10 MHz, and by $C_{\mathrm{ldm}}$ after 10 MHz. $Z_{\mathrm{r}}(s)$ can be determined similar and will not be discussed in detail here.

Due to nonlinearity, if the inductance of the boost PFC changes at different ac current over one period, it does not affect the performance and stability of the active filter. Based on the model, $C_{\mathrm{DM}}$ is in parallel with $L_{\mathrm{boost}}$, and in the concerned frequency range, this parallel impedance is determined by $C_{\mathrm{DM}}$'s impedance. Hence, with the variation of $L_{\mathrm{boost}}$, $G_{\mathrm{OL}}$ is still close to unity in (17) and insertion gain $G_{\mathrm{IFB}}$ is not affected. Hence, the performance is not affected. Moreover, in the loop gain $T_{\mathrm{FB}}$, $L_{\mathrm{boost}}$ is included in $Z_{\mathrm{DM}}/(Z_{\mathrm{DM}} + Z_{\mathrm{R}})$. $Z_{\mathrm{DM}}$ is determined by $L_{\mathrm{DM}}$ in the concerned frequency range. As $C_{\mathrm{DM}}$ is in parallel with $L_{\mathrm{boost}}$, this parallel impedance is determined by $C_{\mathrm{DM}}$'s impedance and is very small compared to $L_{\mathrm{DM}}$, so the stability conditions are not affected.

The active filter does not interact with the main converter because the high impedance of $L_{\mathrm{DM}}$, $L_{\mathrm{CM}}$ and the low impedance of $C_{\mathrm{DM}}$, $C_{\mathrm{R}}$ decouples the active filter from the main converter and LISNs.

In the active filter, $R_G = 100\,\Omega$, $R_F = 1000\,\Omega$, injection capacitor $C_{\mathrm{inj}} = 0.47\,\mu\mathrm{F}$ and the injection resistor $R_{\mathrm{inj}} = 2.5\,\Omega$. $R_{B1}$ and $R_{B2}$ are 4.7 k$\Omega$ and the biasing diodes $\mathrm{D}_1$ and $\mathrm{D}_2$ are 1n4148 high-speed signal diodes. $R_{E1}$ and $R_{E2}$ both are 5-$\Omega$ resistors. For the active filter, the minimum power supply voltage $V_{\mathrm{CC}}$ is the voltage at which the output is on the boundary of being saturated [5]. The saturation voltage is equal to the maximum voltage on the load impedance of the active filter for the injected noise current $I_{\mathrm{inj}}$ plus the voltage drop between base and emitter $V_{\mathrm{BE}}$ and voltage drop in emitter resistance $R_E$. The minimum value of $V_{\mathrm{CC}}$ can be determined by $V_{\mathrm{CC}} \geq I_{\mathrm{inj}} \times (R_E + Z_{\mathrm{inj}} + Z_{\mathrm{CR}}) + V_{\mathrm{BE}}$. In the following experiments, $V_{\mathrm{CC}} = 15\,\mathrm{V}$ has been used.

The chosen OPAM has a power supply noise rejection ratio of 120 dB. And, the class AB amplifiers dc bias condition is not changed by the small noise ripples from the dc power supply, as the diode voltage drop is almost constant for small ripples in dc bias. Hence, the influence of power supply noise can be ignored.

The model of CT was extracted and the HPF $C_{\mathrm{HP}}$ and $R_{\mathrm{CT}}$ are determined in Section III. On the grid side, $Z_r$ includes the LISN and DM capacitor $C_R$'s impedance in parallel, so $Z_r(s) = sL_{\mathrm{LISN}}||R_{\mathrm{LISN}}||\frac{1}{sC_R}$, where $C_R = 0.2\,\mu\mathrm{F}$, $L_{\mathrm{LISN}} = 100\,\mu\mathrm{H}$, and $R_{\mathrm{LISN}} = 100\,\Omega$. Based on these parameters and (10), (11), and (18), the loop gain can be calculated.

To illustrate how the loop gain is measured, in Fig. 24(a), the boost PFC converter is replaced using its Norton equivalence model that has been derived in Fig. 18. The loop gain of the feedback active filter can be measured by breaking the feedback loop between the CT and OPAM in Fig. 24(b). A voltage $V_1$ will be injected to the OPAM at the breaking point. The output voltage $V_2$ of the CT will be measured. The Norton equivalent noise current source should be open during the measurement based on the superposition theory. It means that the PFC converter should be turned OFF but the converter should still be connected to the system, as shown in Fig. 24(b). The measured loop gain will be equal to $V_2/V_1$.

In order to verify the loop gain predicted by the developed model, $S$-parameters $S_{11}, S_{12}, S_{21}$, and $S_{22}$ were measured using network analyzer Copper Mountain Planar 808/1 at the loop breaking point from the input of OPAM to the output of the CT. The measured $S$-parameters were converted to loop gain. Because the lowest frequency which the network analyzer can measure is 100 kHz, the measured loop gain will be from 100 kHz to 30 MHz, whereas the calculated loop gain based on the developed model will be from 10 kHz to 30 MHz.

The measured loop gain is compared with the calculated one in Fig. 25. They match very well from 100 kHz to 30 MHz. There is no comparison below 100 kHz because of the limited frequency range of the network analyzer.

In Fig. 25, there are two unstable frequency ranges due to negative phase margin when the gain is equal to 0 dB. The first one is between 30 and 50 kHz and the other is between 10 and 20 MHz. To validate the identified unstable scenarios, an EMI experiment has been conducted in Fig. 26 using a spectrum analyzer Tektronix RSA306. The switching frequency of the
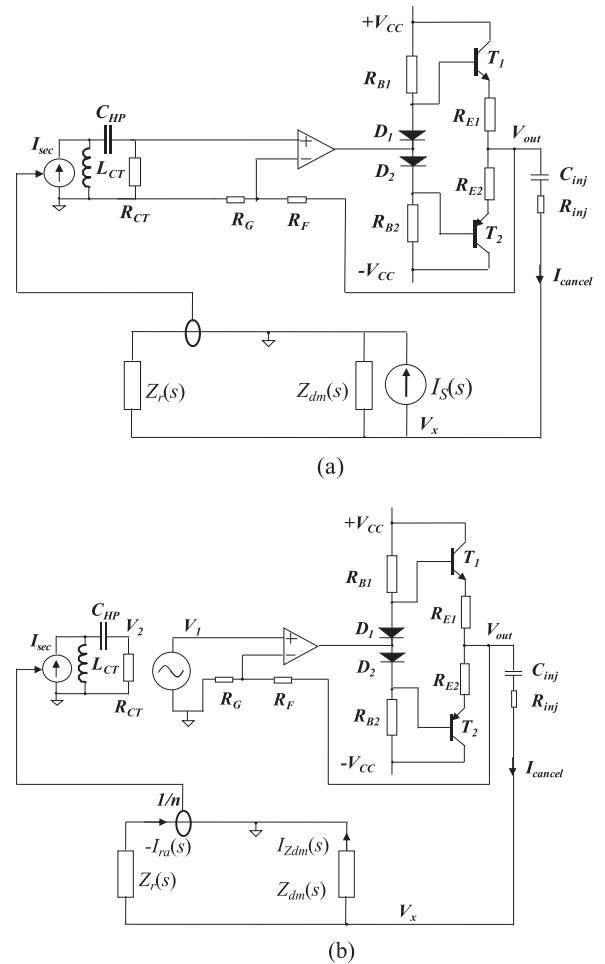


Fig. 24. Loop gain measurement. (a) Feedback active filter with PFC converter DM noise model. (b) Loop gain measurement by breaking the loop.
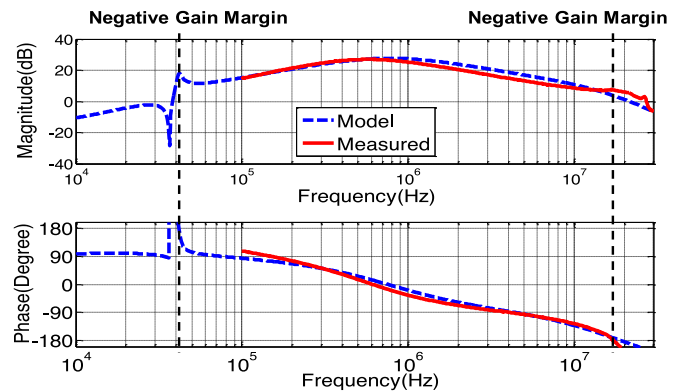


Fig. 25. Comparison of the measured and the modeled loop gains for the uncompensated active filter.

PFC converter is 120 kHz. It has a 120-V ac input, 380-V ouput, and 150-W load.

The measured DM noise curves with and without the feedback active filter are compared in Fig. 27. It is shown in Fig. 27 that there is a small noise bump, although it is not very obvious, around 30–40 kHz, and a big noise bump between 10 and
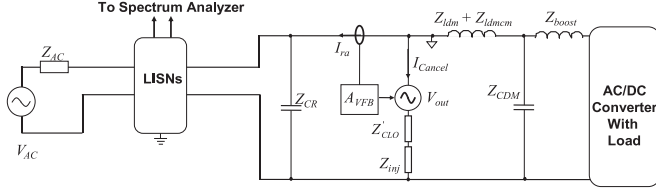
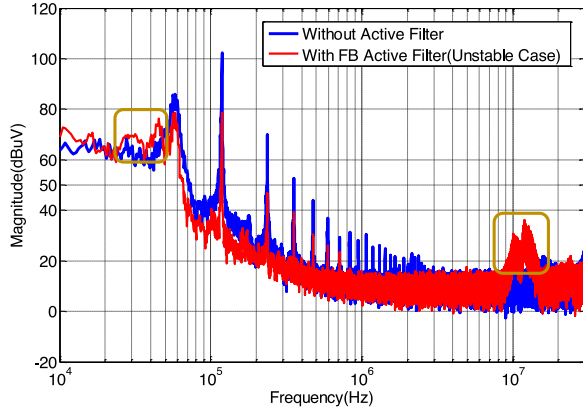Fig. 26. DM noise measurement with an ac source and the ac/dc boost PFC converter.



Fig. 27. Comparison of the measured DM noise curves without and with the uncompensated active filter.
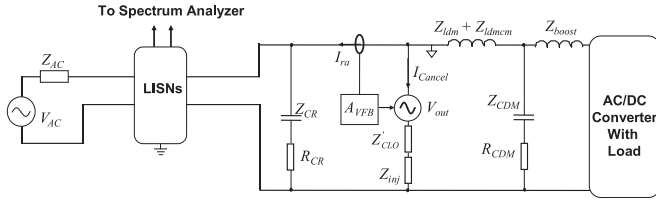


Fig. 28. Adding damping resistances to $C_R$ and $C_{DM}$ to compensate the active filter.

20 MHz as predicted. The instability should be always avoided since it can degrade active filter performance.

### B. Loop Gain Compensation

From the loop gain model of (16), it has been found that the LF gain margin issue is due to the resonances between the inductors and capacitors ($L_{dm} + L_{dmcm}$, $L_{LISN}$, $C_{DM}$, $C_R$). There are two resonances as seen in the loop gain (around 35 and 42 kHz). As there are no damping resistors in the $C_{DM}$ and $C_R$ to damp the resonance, it causes instability. Damping resistors $R_{CDM} = 5\,\Omega$ and $R_{CR} = 1\,\Omega$ are added to damp the responses, as shown in Fig. 28.

The active filter should be compensated to ensure the stability between 10 and 20 MHz. In (16), the OPAM class AB amplifier's voltage gain $A_{VFB}$ is a factor of loop gain. So, it is possible to compensate $A_{VFB}$ to compensate loop gain. In (8), $A_{VFB}$ is the product of the gain of CT-HPF and the gain $A_V$ of OPAM class AB amplifier. So, it is possible to compensate $A_V$ to compensate the loop gain. The $A_V$ in (7) can be further approximately
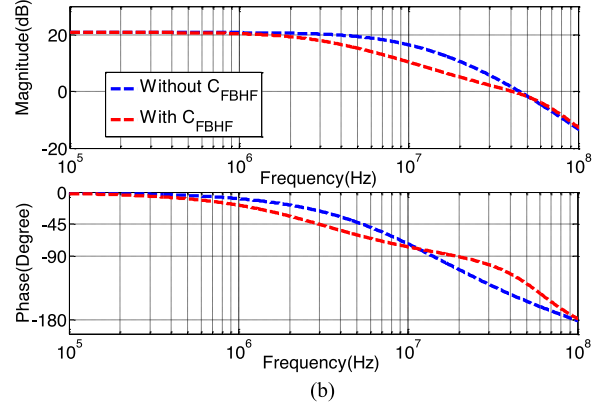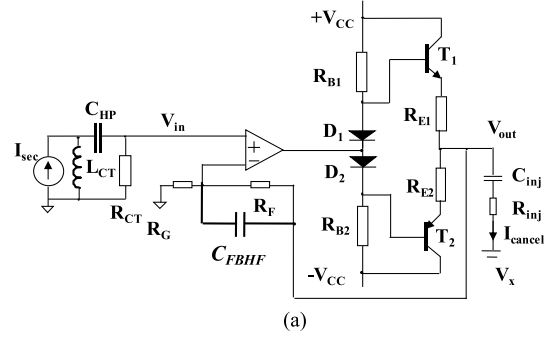


Fig. 29. HF compensations using $C_{FBHF}$: (a) circuit, (b) magnitude and phase of $V_{out}/V_{in}$ without and with $C_{FBHF}$.

simplified to the following equation:

$$A_V = \frac{A_{CLNI}}{1 + \frac{s}{\frac{G_o \omega_1}{A_{CLNI}}} + \left(\frac{s}{\sqrt{\frac{G_o \omega_1 \omega_2}{A_{CLNI}}}}\right)^2} = \frac{A_{CLNI}}{1 + \frac{s}{Q\omega_{NC}} + \left(\frac{s}{\omega_{NC}}\right)^2}$$

(18)

where $\omega_{NC} = \sqrt{\frac{G_o \omega_1 \omega_2}{A_{CLNI}}}$ and $A_{CLNI} = 1 + \frac{R_F}{R_G}$. So, $A_v$ has a double pole $\omega_{NC}$. With the parameters in this paper, the $\omega_{NC}$ is around 15 MHz, which agrees with Fig. 16. Because the double pole has an abrupt $-180°$ change, it makes the phase margin of the loop gain cross over frequency negative. It is possible to split the double pole to two separate single poles, so that the phase will change slowly across 2–3 decades. As a result, there will be enough phase margin at the loop gain's crossover frequency. Based on this, a small capacitance $C_{FBHF} = 30\,pF$ is paralleled with $R_F$ for compensation, as shown in Fig. 29(a). $Z_F$ is now modified as $Z_{F1} = R_F || \frac{1}{sC_{FBHF}}$. With the compensation of $C_{FBHF}$, $A_V$ in (7) is modified as $A_{VC}$

$$A_{VC} = \frac{A_{CLNI} \times \left(1 + \frac{s}{\omega_{ZCMPH}}\right)}{\left(\left(\frac{\left(1 + \frac{s}{\omega_1}\right)\left(1 + \frac{s}{\omega_2}\right)}{G_o}\right)A_{CLNI} \times \left(1 + \frac{s}{\omega_{ZCMPH}}\right) + \left(1 + \frac{s}{\omega_{PCMPH}}\right)\right)}$$

$$\approx \frac{A_{CLNI} \times \left(1 + \frac{s}{\omega_{ZCMPH}}\right)}{(1 + \frac{s}{\omega_{CP1}})(1 + \frac{s}{\omega_{CP2}})(1 + \frac{s}{\omega_{CP3}})}$$
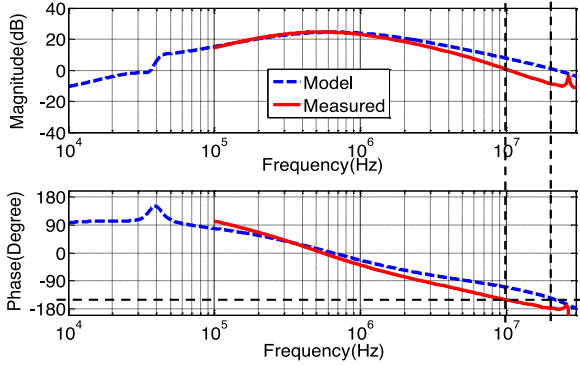
(19)

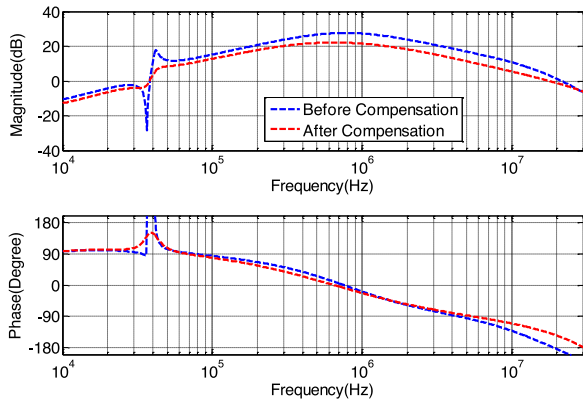Fig. 30. Comparison of measured and modeled loop gains after loop gain compensation.



Fig. 31. Comparison of loop gain math models before compensation and after compensation.

where $\omega_{PCMPH} = \frac{1}{R_F C_{FBHF}}$, $\omega_{ZCMPH} = \omega_{PCMPH}(\frac{R_G + R_F}{R_G})$, $\omega_{CP1} = \frac{1}{(\frac{A_{CLNI}}{G_o \omega_1} + \frac{1}{\omega_{PCMPH}})}$, and $\omega_{CP2} = \omega_2(1 + \frac{G_o \omega_1}{A_{CLNI}\omega_{PCMPH}})$. And with given parameters, $\omega_{ZCMPH}$ is very close to $\omega_{CP3}$, so they cancel each other. The calculated $f_{CP1} \approx 2.9$ MHz and $f_{CP2} \approx 74$ MHz. Fig. 29(b) shows the comparison of $A_V$ and $A_{VC}$. It is shown that with the compensation, around 26° phase leading is achieved around 20 MHz.

The loop gain after compensation was calculated, measured, and compared in Fig. 30. Same as the reason before, due to the frequency range limitation, the measured loop gain starts at 100 kHz. The calculated loop gain can approximately match the measured one.

It is shown in Fig. 30 that both LF and HF stabilities are achieved with compensation. A comparison between the loop gains before and after compensation is shown in Fig. 31. The phase margin is around 40° at crossover frequency around 20 MHz. Based on (16) and Fig. 31, of 40° phase margin, 26° is due to the compensation capacitor $C_{FBHF}$ and 14° is due to the damping resistors $R_{CR}$ and $R_{CDM}$.

In this paper, HF stability issue was clearly identified by analyzing loop gain model equation in HF ranges. This analysis matches the measured loop gain and the instability in the spectral domain. The technique for designing compensation is discussed
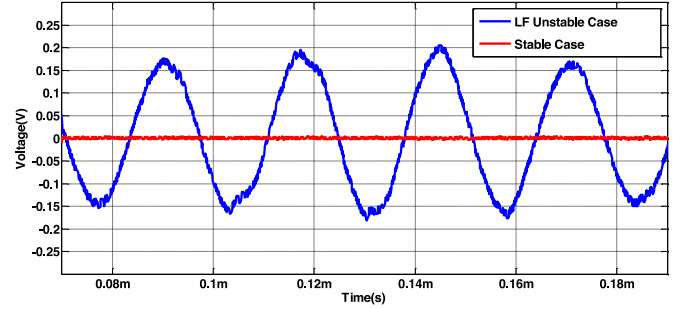


Fig. 32. Time-domain waveforms for LF unstable and stable cases, with HF compensation added in both cases.

and how to improve the phase of the loop gain by compensating the amplifier's voltage gain transfer function using a compensation capacitor $C_{FBHF}$ by splitting the double pole of the transfer function into two separate single poles has been clearly described using the math model. How to design the value of the capacitor based on the desired phase improvement has also been described using equations. In [5], the CM EMI active filter was not modeled. A compensation capacitor was added to improve HF stability, but how it can improve the phase margin of the active filter based on the loop gain model was not discussed. As the relationship between the compensation capacitor of the amplifier and the loop gain of the active filter was not given by any model in [5], how to design the capacitor is unclear.

The stability issues and compensation technique are further validated using time-domain measurements. The measurement setup for these experiments is the same as in Fig. 22(a), except that the converter is not powered and the ac source is also not powered, and only the power supply of the active filter is turned ON. Because the LF and HF stability issues have huge difference in frequency; to identify their effects clearly, three different experiments were conducted. In the first experiment, to find the LF stability issue, at first, LF damping is not added but HF compensation is added. The voltage across the injection resistor $R_{inj}$ is measured and shown in Fig. 32. Without the LF damping resistors $R_{CDM}$ and $R_{CR}$, a resonance waveform of around 37-kHz frequency is shown in Fig. 32. After $R_{CDM}$ and $R_{CR}$ were added, the compensated waveform does not show stability issues.

In the second experiment, at first, HF compensation is not added but LF damping is added. The voltage across the injection resistor $R_{inj}$ is measured and shown in Fig. 33. In the unstable case without the compensation capacitor, a resonance waveform with frequency of around 15 MHz is shown in Fig. 33. After adding the capacitor, compensated waveform does not show stability issues.

In the third experiment, the waveforms when none of the LF or HF compensation is added are shown in Fig. 34 and compared with the stable case.

### C. Insertion Gain and EMI Reduction

Based on the compensated stable loop gain, the insertion gain of the feedback active filter can be calculated based on (17). The
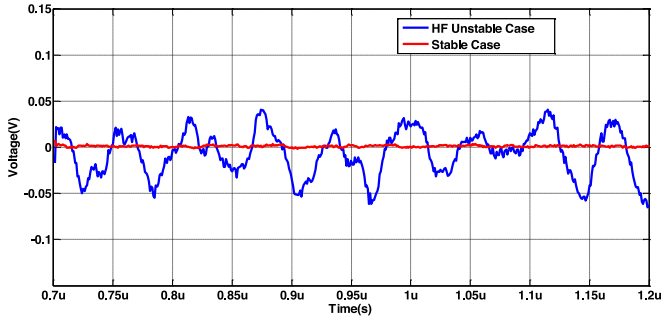
Fig. 33. Time-domain waveforms for HF unstable and stable cases, with LF damping added in both cases.
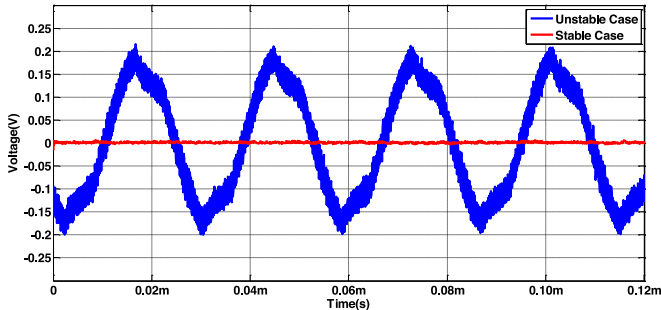


Fig. 34. Time-domain waveforms for unstable case without LF and HF compensation and a stable case with compensation.
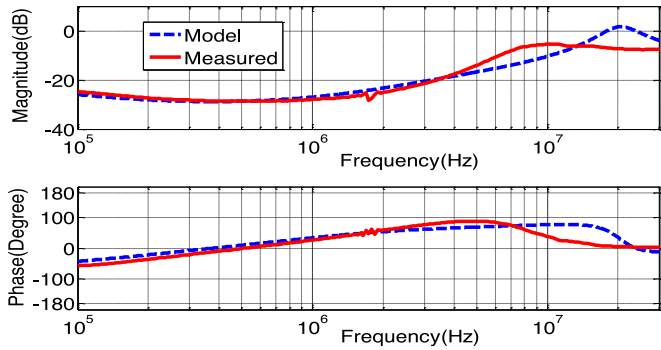


Fig. 35. Comparison of measured and modeled insertion gains for the compensated active filter.
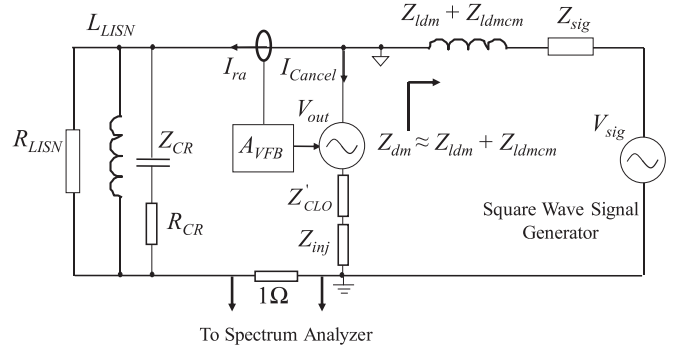


Fig. 36. Noise spectrum measurement setup to verify insertion gain using a square wave signal generator.
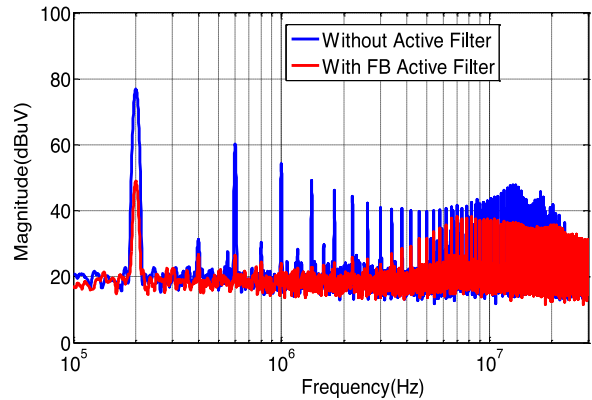


Fig. 37. Noise spectrum comparison without and with the feedback active filter for the setup in Fig. 36.
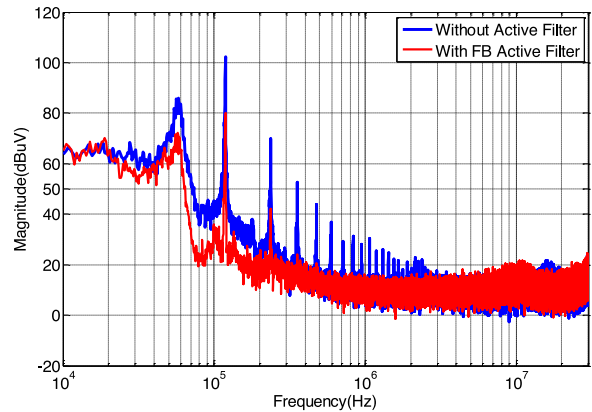


Fig. 38. Measured DM noise spectra without and with the compensated feedback active filter.

insertion gain is also converted using the measured $S$-parameters [16], [27], [28] and compared with the derived model in Fig. 35. They match very well below 10 MHz and have a small difference between 10 and 30 MHz.

To measure the performance of the compensated active filer, two experiments were conducted. In the first experiment, to accurately measure the DM noise current, a 1-$\Omega$ resistance is used in series with the LISNs. Since the impedance of LISNs is much higher than 1 $\Omega$, the voltage drop of the DM current on the 1-$\Omega$ resistance can accurately represent the DM noise current to be measured. The noise source is a square wave signal generator having $Z_{sig} = 50\,\Omega$ source resistance. The signal generator generates a 200-kHz square waveform with an amplitude of $V_{p-p} = 3$ V. The measurement setup is shown in Fig. 36.

The measured noise spectrum with and without the compensated active filter is shown in Fig. 37. It is shown that the active filter is stable in the whole frequency range. Since the impedance of $Z_{ldm} + Z_{ldmcm}$ is much higher than $Z_{sig}$ from 100 kHz to 30 MHz, the noise reduction will be approximately predicted from the measured insertion gain in Fig. 35.

In the second experiment, the DM noise spectra of the ac/dc boost PFC converter without and with the compensated active filter were measured, as shown in Fig. 38. The test setup is the
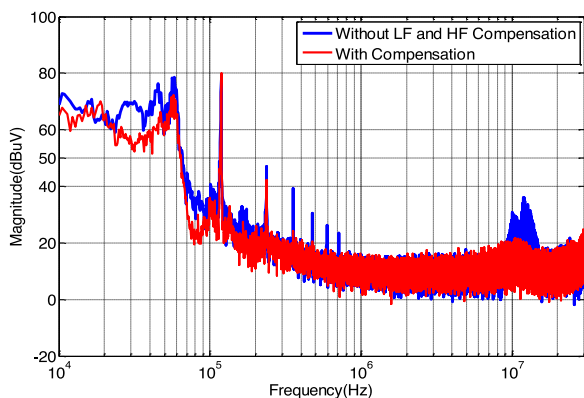
Fig. 39. Comparison of the measured DM noise spectra without and with compensation.

same as Fig. 22(a) but with the compensated active filter (from Figs. 28 and 29). A DM noise separator [33] was connected to the outputs of two LISNs. The output of the noise separator was connected to the spectrum analyzer for EMI measurement. The input voltage of the PFC converter is 120-V ac with 150-W load and 120-kHz switching frequency. Compared to the measured EMI for unstable case in Fig. 27, the active filter is stable within the whole frequency range. There are no noise spikes observed due to the instability of the active filter. Also, the noise reduction agrees with the measured and calculated insertion gains in Fig. 35. On the other hand, in Fig. 27, the noise reduction was less than expected from the insertion gains in Fig. 35 due to instability.

Fig. 39 shows the comparison of the measured DM EMI noise for the boost PFC converter with the uncompensated active filter and with the compensated active filter. This figure shows how the LF and HF bumps of the uncompensated case, which were caused by the instability, are not present in the compensated case. It also shows that, for the compensated case, the noise reduction is very close to what is expected from Fig. 35, as with the compensation, the active filter can work properly.

## VI. CONCLUSION

In this paper, the model of a current sensing-current feedback DM active filter is investigated for ac/dc power converters. The models of active filter components are explored in detail. Based on the developed component models, the model of the active filter, which includes a CT, an HPF, an OPAM, and a class AB amplifier, is developed. The system model, which includes the noise source impedance of an ac/dc converter, the feedback active filter model, and the load of active filter, is developed. The loop gain and insertion gain of the feedback active filter system is studied. Based on the developed loop gain and insertion gain, the feedback active filter's stability and EMI reduction performance are investigated. A compensation technique is applied to the active filter to achieve stability. Both simulations and experiments have proved that the developed techniques can correctly model the active filter system. The loop gain model can correctly predict the stability of the active filter system and the insertion gain model can correctly predict the EMI reduction performance

of the active filter. With the developed modeling technique, the active filter can be compensated to achieve stability and good noise reduction.

## REFERENCES

[1] C. R. Paul, *Introduction to Electromagnetic Compatibility*. 2nd ed. Hoboken, New Jersey, USA: Wiley, 2006.

[2] G. Ala, G. C. Giaconia, G. Giglia, M. C. Di Piazza, and G. Vitale, "Design and performance evaluation of a high power-density EMI filter for PWM inverter-fed induction-motor drives," *IEEE Trans. Ind. Appl.*, vol. 52, no. 3, pp. 2397–2404, May–Jun. 2016.

[3] M. Hartmann, H. Ertl, and J. W. Kolar, "EMI filter design for a 1 MHz, 10 kW three-phase/level PWM rectifier," *IEEE Trans. Power Electron.*, vol. 26, no. 4, pp. 1192–1204, Apr. 2011.

[4] K. Mainali and R. Oruganti, "Conducted EMI mitigation techniques for switch-mode power converters: A Survey," *IEEE Trans. Power Electron.*, vol. 25, no. 9, pp. 2344–2356, Sep. 2010.

[5] S. Wang, Y. Y. Maillet, F. Wang, D. Boroyevich, and R. Burgos, "Investigation of hybrid EMI filters for common-mode EMI suppression in a motor drive system," *IEEE Trans. Power Electron.*, vol. 25, no. 4, pp. 1034–1045, Apr. 2010.

[6] J. Biela, A. Wirthmueller, R. Waespe, M. L. Heldwein, K. Raggl, and J. W. Kolar, "Passive and active hybrid integrated EMI filters," *IEEE Trans. Power Electron*, vol. 24, no. 5, pp. 1340–1349, May 2009.

[7] M. Ali, E. Laboure, and F Costa, "Integrated active filter for differential-mode noise suppression," *IEEE Trans. Power Electron.*, vol. 29, no. 3, pp. 1053–1057, Mar. 2014.

[8] W. Chen, X. Yang, and Z. Wang, "A novel hybrid common-mode EMI filter with active impedance multiplication," *IEEE Trans. Ind. Electron.*, vol. 58, no. 5, pp. 1826–1834, May 2011.

[9] M. C. Di Piazza, A. Ragusa, and G. Vitale, "Design of grid-side electromagnetic interference filters in AC motor drives with motor-side common mode active compensation," *IEEE Trans. Electromagn. Compat.*, vol. 51, no. 3, pp. 673–682, Aug. 2009.

[10] C. Zhu and T. H. Hubing, "An active cancellation circuit for reducing electrical noise from three-phase AC motor drivers," *IEEE Trans. Electromagn. Compat.*, vol. 56, no. 1, pp. 60–66, Feb. 2014.

[11] D. Hamza, M. Sawan, and P.K. Jain, "Suppression of common-mode input electromagnetic interference noise in DC-DC converters using the active filtering method," *IET Trans. Power Electron.*, vol. 4, no. 7, pp. 776–784, Aug. 2011.

[12] M. C. Di Piazza, M. Luna, and G. Vitale, "EMI reduction in DC-fed electric drives by active common-mode compensator," *IEEE Trans. Electromagn. Compat.*, vol. 56, no. 5, pp. 1067–1076, Oct. 2014.

[13] D. Shin *et al.*, "Analysis and design guide of active EMI filter in a compact package for reduction of common-mode conducted emissions," *IEEE Trans. Electromagn. Compat.*, vol. 57, no. 4, pp. 660–671, Aug. 2015.

[14] X. Chang, W. Chen, Y. Yang, K. Wang, and X. Yang, "Research and realization of a novel active common-mode EMI filter," in *Proc. IEEE Appl. Power Electron. Conf. Expo.*, 2015, pp. 1941–1945.

[15] K. Mainali and R. Oruganti, "Design of a current-sense voltage-feedback common mode EMI filter for an off-line power converter," in *Proc. IEEE Power Electron. Spec. Conf.*, 2008, pp. 1632–1638.

[16] Y. Chu, S. Wang, and Q. Wang, "Modeling and stability analysis of active/hybrid common-mode EMI filters for DC/DC power converters," *IEEE Trans. Power Electron.*, vol. 31, no. 9, pp. 6254–6263, Sep. 2016.

[17] W. Chen, W. Zhang, X. Yang, Z. Sheng, and Z. Wang, "An experimental study of common- and differential-mode active EMI filter compensation characteristics," *IEEE Trans. Electromagn. Compat.*, vol. 51, no. 3, pp. 683–691, Aug. 2009.

[18] P. Cantillon-Murphy, T.C. Neugebauer, C. Brasca, and D. J. Perreault, "An active ripple filtering technique for improving common-mode inductor performance," *IEEE Power Electron. Lett.*, vol. 2, no. 2, pp. 45–50, Jun. 2004

[19] M. Zhu, D. J. Perreault, V. Caliskan, T. C. Neugebauer, S. Guttowski, and J. G. Kassakian, "Design and evaluation of feedforward active ripple filters," *IEEE Trans. Power Electron.*, vol. 20, no. 2, pp. 276–285, Mar. 2005

[20] D. C. Hamill, "An efficient active ripple filter for use in DC-DC conversion," *IEEE Trans. Aerosp. Electron. Syst.*, vol. 32, no. 3, pp. 1077–1084, Jul. 1996.

[21] T. Farkas and M. F. Schlecht, "Viability of active EMI filters for utility applications," *IEEE Trans. Power Electron.*, vol. 9, no. 3, pp. 328–337, May 1994.

[22] R. Goswami, S. Wang, and Y. Chu, "Modeling and analysis of hybrid differential mode filters for AC/DC converters to suppress current ripples and EMI," in *Proc. IEEE Energy Convers. Congr. Expo.*, pp. 2429–2436, Sep. 20–24, 2015

[23] D. Hamza, M. Pahlevaninezhad, and P. K. Jain, "Implementation of a novel digital active EMI technique in a DSP-based DC–DC digital controller used in electric vehicle (EV)," *IEEE Trans. Power Electron.*, vol. 28, no. 7, pp. 3126–3137, Jul. 2013.

[24] K. Raggl, T. Nussbaumer, and J.W. Kolar, "Guideline for a simplified differential-mode EMI filter design," *IEEE Trans. Ind. Electron.*, vol. 57, no. 3, pp. 1031–1040, Mar. 2010.

[25] Z. Wang, S. Wang, P. Kong, and F. C. Lee, "DM EMI noise prediction for constant on-time, critical mode power factor correction converters," *IEEE Trans. Power Electron.*, vol. 27, no. 7, pp. 3150–3157, Jul. 2012.

[26] Z. Wang, S. Wang, C. Wang, F. C. Lee, and P. Kong, "DM EMI noise prediction in constant on-time PFC," in *Proc. IEEE Energy Convers. Congr. Expo.*, San Jose, CA, USA, 2009, pp. 3437–3442.

[27] S. Wang, F. C. Lee, and W. G. Odendaal, "Characterization and parasitic extraction of EMI filters using scattering parameters," *IEEE Trans. Power Electron.*, vol. 20, no. 2, pp. 502–510, Mar. 2005.

[28] S. Wang, F. C. Lee, and W. G. Odendaal, "Using scattering parameters to characterize EMI filters," in *Proc. IEEE 35th Annu. Power Electron. Spec. Conf.*, 2004, pp. 297–303.

[29] AD829 Datasheet, AD829 IC, high speed, low noise audio Op Amp, 2011, Analog Devices, Inc., Norwood, MA, USA.

[30] R. C. Jaeger, *Microelectronic Circuit Design*. Boston, MA, USA: McGraw-Hill, 1997.

[31] S. Wang, F. C. Lee, and W. G. Odendaal, "Improving the performance of boost PFC EMI filters," in *Proc. 18th Annu. IEEE Appl. Power Electron. Conf. Expo.*, Miami Beach, FL, USA, 2003, vol. 1, pp. 368–374.

[32] S. Wang, F. C. Lee, and W. G. Odendaal, "Single layer iron powder core inductor model and its effect on boost PFC EMI noise," in *Proc. IEEE 34th Annu. Power Electron. Spec. Conf.*, 2003, vol. 2, pp. 847–852.

[33] S. Wang, F. C. Lee, and W. G. Odendaal, "Characterization, evaluation, and design of noise separator for conducted EMI noise diagnosis," *IEEE Trans. Power Electron.*, vol. 20, no. 4, pp. 974–982, Jul. 2005.

[34] A. Ragusa, P. Zanchetta, L. Empringham, L. De Lillo, and M. Degano, "High frequency modelling method of EMI filters for hybrid Si - SiC matrix converters in aerospace applications," in *Proc. 28th Annu. IEEE Appl. Power Electron. Conf. Expo.*, Long Beach, CA, USA, 2013, pp. 2610–2617.

[35] T. Farkas, "A scientific approach to EMI reduction," M.S. thesis, Massachusetts Inst. Technol., Cambridge, MA, USA, Aug. 1991.

**Rajib Goswami** (S'11) received the B.Sc. and M.Sc.degrees in 2009 and 2012, respectively, both in electrical and electronic engineering from Bangladesh University of Engineering and Technology, Dhaka, Bangladesh, and the Ph.D. degree in electrical engineering from the University of Texas at San Antonio, TX, USA, in December 2017.

From 2010 to 2012, he was an Electrical and Electronics Engineer with the Bangladesh Atomic Energy Commission. He was a Research Intern with the Power Electronics and Electrical Power Research Laboratory, University of Florida. His research interests include hybrid (active/passive) EMI filter design for DM/CM noise of power converters, EMI noise analysis and filter design for three-phase converters, power conversion from wind turbine generators (maximum power tracking), etc.
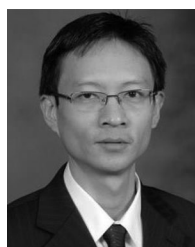
**Shuo Wang** (S'03–M'06–SM'07) received the Ph.D. degree from Virginia Tech, Blacksburg, VA, USA, in 2005.

Since 2015, he has been an Associate Professor with the Department of Electrical and Computer Engineering, University of Florida, Gainesville, FL, USA. From 2010 to 2014, he was with the University of Texas at San Antonio, TX, USA, first as an Assistant Professor and later as an Associate Professor. From 2009 to 2010, he was a Senior Design Engineer with the GE Aviation Systems, Vandalia, OH, USA. From 2005 to 2009, he was a Research Assistant Professor with the Virginia Tech. He has authored or coauthored more than 150 IEEE journal and conference papers and holds 8 US patents.

Dr. Wang is an Associate Editor for the IEEE TRANSACTIONS ON INDUSTRY APPLICATIONS and a Technical Program Co-Chair for the IEEE 2014 International Electric Vehicle Conference. He was the recipient of the Best Transaction Paper Award from the IEEE Power Electronics Society in 2006 and two William M. Portnoy Awards for the papers published in the IEEE Industry Applications Society in 2004 and 2012, respectively. He was also the recipient of the prestigious National Science Foundation CAREER Award in 2012.